# Modelling and effects of fuel radiation in methanol pool fires

Jean-Louis Consalvi, Fatiha Nmira, Frédéric André

# Modelling and effects of fuel radiation in methanol pool fires

Jean-Louis Consalvi[a*], Fatiha Nmira[b], Frédéric André[c]

[a]Aix-Marseille Université, IUSTI UMR 7343, 5 rue E. Fermi, 13543 Marseille cedex 13, jean-louis.consalvi@univ-amu.fr

[b]Direction R&D EDF, 6 Quai Watier, 78401, Chatou Cedex, France, fatiha.nmira@edf.fr

[c]Univ Lyon, CNRS, INSA-Lyon, Université Claude Bernard Lyon 1, CETHIL UMR5008, F-69621 Villeurbanne, France, frederic.andre@insa-lyon.fr

*Corresponding author

**Abstract:**

This article proposes a computationally affordable radiative heat transfer model to predict accurately the feedback toward the fuel surface. It combines the multi-scale full-spectrum k (MSFSK) approach to model accurately the radiative interaction between $CO_2$/$H_2O$ and the fuel and the rank correlated (RCFSK) scheme. The model achieves the narrow band correlated-k model accuracy with only five quadrature points for each of the two scales. The predictions are also weakly dependent on the Planck temperature which allows to store efficiently the MSRCFSK parameters in a flamelet library. The model is implemented in a well-validated numerical model to provide large eddy simulations of 30 cm and 1 m diameter methanol pool fires. The heat feedback predictions are improved when methanol radiation is considered. The overall radiative contribution of methanol results from two competitive mechanisms: an increase in emission in the hot part of the fuel dome and an increase in absorption close to the pool surface. For both pool fires, the enhancement in emission overall dominates, leading to higher radiative loss and heat feedback. The contribution of absorption increases with the pool size and, as a result, the effects of methanol radiation are more pronounced for the 30 cm pool than for the 1 m one.

**Keywords:** radiative heat transfer; modeling; fuel dome; methanol pool fires; multi-scale rank-correlated full-spectrum k

## 1. Introduction

The pyrolysis and the burning rate of solid and liquid fuels in fire scenarios are mainly controlled by the complex radiative feedback from the flame to the condensed fuel surface [1]. This feedback results from the transport of the radiation through the fuel rich core of the flames that contains a significant amount of fuel or hydrocarbon vapors [2,3]. A prerequisite to its modelling is then a detailed characterization of the radiative properties of the gaseous species of interest, including combustion products and hydrocarbon fuels, at high spectral resolution and temperatures relevant for fire applications. Such data are available for water vapor, carbon dioxide, carbon monoxide and methane in the spectroscopic database HITEMP 2010 [4]. The line parameters for some other typical hydrocarbon fuels encountered in fire applications are also available in the HITRAN spectroscopic database [5]. However, some important bands are missing for these fuels and this spectroscopic database cannot be used with confidence above 600 K [6]. On the other hand, the National Institute of Standards and Technology (NIST)

reported FTIR transmission measurements for nine gaseous fuels, including paraffins (methane, ethane, propane, and n-heptane) and other fuels (methanol, ethylene, propylene, toluene, and methyl-methacrylate), at a spectral resolution of 1 $cm^{-1}$ and over a temperature range from 300 K to 1000 K [2,7]. These data were used to derive databases of statistical narrow band (SNB) model parameters [6,8].

The development LES-based fire simulators raised naturally the issue of the engineering gas radiative modelling for fire applications. However, very few studies have tried to extend state-of-the-art engineering radiative property models to account for fuel radiation. Sadeghi et al. [9] derived weighted-sum-of-grey-gases (WSGG) parameters for the nine fuels of the NIST database, carbon monoxide and soot and applied the superposition scheme to generate the WSGG parameters for mixtures of $CO_2$, $H_2O$, CO, hydrocarbon fuel and soot. The model was validated in decoupled radiative calculations by comparison with line-by-line (LBL) simulations. However, the use of the superposition scheme, that results in $N_{RTE} = N_s \times \left(N_g + 1\right)$ radiative transfer equation (RTE) to solve where $N_S$ is the number of species and $N_g \sim 4$ is the number of grey gases for a given species, makes this approach time consuming and probably unaffordable for LES applications. On the other hand, global non-grey models based on the k-distribution concept, such as the Full-Spectrum Correlated-k (FSCK) or the Spectral Line based Weighted-Sum-of-Grey-Gases (SLW) [10], combine accuracy and computational efficiency and are good candidate to be applied in LES of fire scenarios (see Refs. [11-13] for example). These models lie on the assumption of correlated spectrum to deal with non-homogeneous non-isothermal medium. However, this assumption no longer holds in the radiative feedback scenario where the radiation emitted by a gas/particle mixture is absorbed by another gas [14,15]. Modest and co-workers introduced the multi-scale FSCK approach to model accurately the radiative heat transfer in such configurations [14, 15]. The approach consists in separating the contributions of the $M$ different radiatively participating species, called scales, to the absorption coefficient. Consalvi and Liu applied the MSFSCK to decoupled radiation calculations in methane fire plumes of different heat release rates by considering two scales, one for the $CO_2$/$H_2O$/soot mixture and the other one for methane [16]. This results in $N_{RTE} = 2 \times N_g$ RTE to be solved where $N_g$ is the number of quadrature points. The MSFSCK was found to provide a good agreement with LBL solutions. However, no attempt was made to implement this model for LES of fire scenarios.

The objective of this article is twofold: (i) to optimize the MSFCSK to be implemented in LES-based fire simulators, (ii) to investigate the role of methanol radiation in the well-documented 30 cm and 1 m methanol pool fires investigated experimentally in Refs. [17-19] and [20,21].

## 2. Methanol pool fires

The target pool fires considered in the present study are the well-documented 30 cm and 1 m diameter methanol pool fires investigated experimentally in Refs. [17-19] and [20,21], respectively. These pool fires are also target flames in the MacFP workshop [22]. We performed LES of these flames in previous studies with the numerical model described in Section 3 by disregarding methanol radiation [11,12]. These simulations were performed with Code_Saturne developed at EDF [23]. Our numerical results were found to reproduce with fidelity the experimental data in terms of puffing frequency, flame structure and radiative outputs, although

the radiative feedback was underestimated in both cases. Table 1 summarizes the pool fire characteristics, including the pool diameter, $D$, and the Heat Release Rate (HRR), $\dot{Q}$.

Table 1. Target methanol flames and computational grids. *z* represents the vertical direction.

| **Diameter, $D$ (m)** | **HRR ($\dot{Q}$, kW)** | **Mesh** |
|---|---|---|
| 0.30 | 22.45 | Computational domain: 3×3 ×3 $m^3$<br>$\Delta_x = \Delta_y = \Delta_z$ = 2.5 mm for 0.4×0.4×0.2 m<br>and $\Delta_z$ =5 mm for 0.2m ≤ z ≤ 0.6m |
| 1.00 | 269 | Computational domain: 9×9 ×7 $m^3$<br>$\Delta_x$ = 8.15 mm; $\Delta_y$ = 8.15 mm; $\Delta_z$ = 5 mm for 0.6×0.6×0.01 m<br>$\Delta_z$ stretched from z = 0.01 m to z = 0.326 m<br>$\Delta_z$ = 1.58 cm from z = 0.326 m to z = 1.8 m |

## 3. Description of the numerical model and computational details

A detailed description of the model was reported in the previous articles [11,12]. The numerical model solves the filtered transport equations of mass, momentum, enthalpy, mixture fraction and second moment of mixture fraction. The subgrid-scale momentum stress and scalar flux are computed using a dynamic Smagorinsky model and a dynamic eddy diffusivity model, respectively. A non-adiabatic steady laminar flamelet is considered to provide state relationships for thermophysical properties as a function of the mixture fraction, $Z$, scalar dissipation rate, $\chi$, and enthalpy defect, $X_R$. The flamelet library is generated by solving the governing equations of counterflow diffusion flames in the physical space with the oxidation mechanism of Li et al. [24]. The Favre-filtered thermochemical quantities are then obtained from the state relationships by convolution with a presumed Filtered Density Function (FDF). Z, $\chi$ and $X_R$ are assumed to be statistically independent and the marginal FDFs are modelled by a $\beta$-distribution for $Z$ and $\delta$-distributions for $\chi$ and $X_R$:

$$\tilde{\phi} = \iiint \phi^{fl}(Z,\chi,X_R)\beta\left(Z;\ \tilde{Z},V_z\right)\delta(\chi-\tilde{\chi})\delta\left(X_R-\widetilde{X_R}\right) \quad (1)$$

Where the superscript *fl* refers to the flamelet library and $V_z$ is the subgrid scale (SGS) mixture fraction variance. The variance is calculated from its definition, $V_z = \widetilde{Z^2} - \tilde{Z}^2$, by using a transport equation for the second moment of the mixture fraction. The filtered scalar dissipation rate, $\tilde{\chi}$, is computed by the model proposed by Jiménez et al. [25], $\tilde{\chi} = \frac{\tilde{D}+D_t}{C_I\Delta^2}V_z$, with $C_I$ computed by a dynamic approach. The Favre-filtered thermochemical quantities are then stored in a library as function of $\tilde{Z}, V_z$, $\tilde{\chi}$ and $\widetilde{X_R}$ and are interpolated during the simulations based on the local values of these parameters.

The computational domains and grids for both the 30 cm and 1 m methanol pools are the same as in Refs. [11,12] and are summarized in Table 1. For all the simulations, the computational domain is bounded by open boundaries at the top and sides and typical convective and outflow/inflow conditions are applied, respectively. At the inlet, a spatially uniform and steady velocity is imposed to provide the mean HRR specified experimentally during the steady burning

and both convective and diffusive mass and energy fluxes are considered. The inlet temperature is set to the boiling point of methanol, i.e. $T_b$ =338 K. A great attention was put to mimic the experimental burner boundary conditions as it was demonstrated that they significantly affect the flame dynamics [11]. In the rest of the domain, the classical wall boundary condition is imposed.

## 4. Radiative property modelling

### 4.1 High resolution absorption spectra

Absorption spectra are required to generate the corresponding databases or model coefficients. For $CO_2$ and $H_2O$, the detailed spectral absorption cross-section database, generated by Pearson et al. [26] from HITEMP 2010 [4], is considered. This database covers the entire thermal spectrum ($\eta \in [0 - 25{,}000\ \mathrm{cm}^{-1}]$ where $\eta$ is the wavenumber) with a resolution of 0.005 $cm^{-1}$ for temperatures ranging from 300 to 3000 K. For methanol, the spectral absorption coefficients were obtained from the FTIR measurements performed at NIST by Wakatsuki et al. [7] between 700 and 4000 $cm^{-1}$ with a resolution of 1 $cm^{-1}$ at seven temperatures ranging from 295 K to 1000 K, with 1000 K being close to the temperature (≈1100 K) at which the fast pyrolysis of most hydrocarbons occurs.

### 4.2 Narrow band calculations

Narrow band calculations, based on the narrow-band correlated k (NBCK) model, will be used as reference solution in decoupled calculations.

The first step to perform the simulations is to generate a database of narrow band (NB) k-g distributions. This NB database will also serve as starting points to generate the Full-spectrum k-g distributions (see Section 4.3). For each radiating gaseous species, a database of NB k-g distributions, denoted $g^{NB}$ hereafter, was generated for 128 values of $g$ corresponding to a 128-point Gauss quadrature scheme, 9 mole fractions, $x$, ranging between 0 and 1 (0, 0.05, 0.1, 0.2, 0.3, 0.4, 0.6, 0.8, 1), 28 temperatures, $T$, ranging from 300 to 3000 K (by a uniform step of 100 K), and $n_{NB} = 998$ narrow bands with a resolution of $\Delta\eta = 25$ $cm^{-1}$. For $CO_2$ and $H_2O$, the NB k-g distributions were directly generated from the LBL spectral absorption cross-section database of Pearson [26]. For $CH_3OH$, the parameters of the Malkmus Statistical Narrow Band (SNB) model $\bar{k}$ and $\beta$ were first derived for each NB and temperature from the high-resolution FTIR measurements by using the methodology proposed in Ref. [27]. These parameters were found in close agreement with those derived in Ref. [6] by using a different method. These narrow band model parameters were used to obtain the NB k-g distributions through the inversion of the cumulative density function [28]:

$$g^{NB}(k) = \frac{1}{2}\left[1 - \mathrm{erf}\left(\frac{a}{\sqrt{k}} - b\sqrt{k}\right)\right] + \frac{1}{2}\left[1 - \mathrm{erf}\left(\frac{a}{\sqrt{k}} + b\sqrt{k}\right)\right] \quad (2)$$

where $a = \sqrt{xp\beta\bar{k}/2\pi}$ and $b = \sqrt{\beta/2\pi xp\bar{k}}$ with $p$ the total pressure. This inversion is performed through a Newton-Raphson iteration method.

Decoupled NB calculations are then performed by using the procedure proposed by Modest and Riazzi [29]: i) at each computational grid node, single species NB k-g distributions at the local thermodynamic states are obtained from the database for each NB and each of the 128 Gauss-point by linear interpolations on both $x$ and $T$. ii) These single species NB k-g distributions are mixed by using the mixing scheme of Modest and Riazzi [29]. iii) Finally, for each NB, the

absorption coefficients at the 10 Gauss points used to solve the NB RTE are obtained from the mixed 128 Gauss-point NB k-g distributions by using a linear interpolation.

### 4.3 Full-spectrum k-distribution models

*4.3.1 Rank-correlated full-spectrum k distribution model*

Full-spectrum k-distribution (FSK) models introduce a Planck-weighted cumulative k-g distribution, defined as [9]:

$$g^{FS}\left(k,\phi,T_p\right)=\frac{\int_0^{+\infty}H\left[k-\kappa_\eta(\phi)\right]I_{b\eta}(T_p)d\eta}{I_b(T_p)} \quad (3)$$

where $T_p$, H, $k$, $\kappa_\eta$, $I_b$ and $\phi=\{T,x_{CO2},x_{H2O},x_F\}$ are the Planck temperature, the Heaviside function, a given value of the absorption coefficient, the spectral absorption coefficient at $\eta$, the blackbody intensity and an array of variables affecting the absorption coefficient. $x_F$ represents the fuel vapor mole fraction. The FS RTE is expressed as [9]:

$$\frac{dI_{g0}}{ds}=k^\star(g_0)a(g_0)I_b(T)-k^\star(g_0)I_{g0} \quad (4)$$

where $g_0$ corresponds in the present study to a quadrature-point of a Gauss-Legendre quadrature scheme and $I_{g0}$ is the radiative intensity at this quadrature point [9]. In the present study, the RCFSK scheme is considered to determine the absorption coefficient, $k^\star$, and the stretching function, $a(g_0)$ [30]:

$$g^{FS}\left(k^\star,\phi,T_p\right)=g_0 \quad (5)$$

$$a(g_0)=\frac{\partial g^{FS}(k^\star,\phi,T)}{\partial g_0} \quad (6)$$

The procedure proposed by Modest and Riazzi [29] is used to obtain the FS k-g distributions required to solve Eqs. 5 and 6. The two first steps (i and ii) are the same as for the NB calculations (see Section 4.2). The third step consists in assembling the 128-Gauss point mixed FS k-g distributions from the 128-Gauss point mixed NB k-g distributions:

$$g^{FS}\left(k,\phi,T_p\right)=\sum_{all\ NB}\frac{I_{b\eta}(T_p)}{I_b(T_p)}g^{NB}(k,\phi) \quad (7)$$

*4.3.2 Multi-scale rank-correlated full-spectrum k distribution model*

The presence of the fuel vapor induces strong inhomogeneities in the composition of species mixtures and, as a result, the assumption of rank-correlated absorption coefficient, on which the RCFSK model lies, is no longer valid. This can produce inaccurate predictions of radiative heat transfer. In order to correct this deficiency, Modest and co-workers proposed the multi-scale FSK (MSFSK) [14,15]. This model is described briefly here and, in the present formulation, is coupled to the RCFSK scheme proposed in Ref. [30], leading to a model weakly sensitive to the choice of the Planck temperature. This model will be referred to as the MSRCFSK hereafter. The MSFSK consists of separating the contributions of the *M* different radiatively participating species, called scales, to the absorption coefficient. Two scales are considered in the present study consistently with the problem under consideration [16]. The first, referred to as $mix$ hereafter, combines $CO_2$ and $H_2O$ whereas methanol, denoted by a subscript $F$ hereafter, is

treated as a second scale. The spectral RTE is then transformed into two component RTEs, one for each scale and the reordering of the absorption coefficient is applied to each scale leading to two FS RTEs:

$$\frac{dI_{mix,g_0}}{ds} = k^{\star}_{mix}(g_0)a_{mix}(g_0)I_b(T) - \lambda_{mix}(g_0)I_{mix,g_0} \tag{8a}$$

$$\frac{dI_{F,g_0}}{ds} = k^{\star}_{F}(g_0)a_{F}(g_0)I_b(T) - \lambda_{F}(g_0)I_{F,g_0} \tag{8b}$$

$k^{\star}$ and $a$ for both the mixture and methanol scales are determined from Eqs. 5 and 6. Following Modest and co-workers [14,15], the overlap parameters, $\lambda$, are evaluated in an approximate way, such that the emitted intensity emanating from a homogeneous slab bounded by black wall is predicted exactly [14,15]. They demonstrated that a generic expression can be obtained for the determination of the overlap parameter $\lambda_m$ of the m$^{th}$ scale based on the NB k-distributions of individual species [14,15]:

$$\sum_{i=1}^{n_{NB}} \frac{I_{bi}}{I_b} \int_0^{g_{m,i}^{NB}(k_m)} k_{m,i}\, dg_{m,i} = \sum_{i=1}^{n_{NB}} \frac{I_{bi}}{I_b} \int_{g_{1,i}^{NB}=0}^{1} \cdots \int_{g_{M,i}^{NB}=0}^{1} k_{m,i}\, \mathrm{H}\left(\lambda_m - \sum_{i=1}^{M} k_{n,i}\right) dg_{1,i} \cdots dg_{M,i} \text{ for } m = 1, \cdots, M \tag{9}$$

where $I_{bi} = \int_{\Delta\eta} I_{b\eta} d\eta$. The number of RTEs to solve in the MSRCFSK method is equal to $N_g \times M\ (= 2)$, where $N_g$ is the order of the Gaussian quadrature scheme. It should be pointed out that the MSRCSFK reduces to the RCFSK method when no fuel is present.

### 4.4 Evaluation and optimization in decoupled calculations

*4.4.1 Temperature and radiating species mole fraction profiles*

The MSRCFSK will be assessed and optimized through decoupled radiation calculations along line of sight corresponding to the fire plume axis. The RTE is solved along this line of sight from a far location in the inert plume toward the pool surface. The corresponding input temperature and species mole fractions are obtained from the LES calculations performed without considering fuel radiation [11,12]. A zoom of these profiles in the fuel rich core is displayed in Fig. 1. They were found in quantitative agreement with the experimental ones (see section S1 of the supplementary materials). The axial distance is normalized by $\dot{Q}^{2/5}$ to collapse roughly the temperature and species mole fraction profiles. Temperature and $CO_2$ and $H_2O$ mole fractions are roughly constant in the fuel rich core, except close to the fuel surface ($z/\dot{Q}^{2/5} \leq$0.01 kW/m$^{2/5}$) where they increase sharply with $z/\dot{Q}^{2/5}$. As expected, the fuel mole fraction decreases sharply with $z/\dot{Q}^{2/5}$ because of the fuel pyrolysis. The fuel dome can then be decomposed into a hot region with mean temperature higher than 1000 K ($z/\dot{Q}^{2/5} >$0.01 kW/m$^{2/5}$) and a cooler region containing mainly fuel vapor at the vicinity of the fuel surface ($z/\dot{Q}^{2/5} \leq$0.01 kW/m$^{2/5}$).

*4.4.2 Narrow-band calculations*

The left frames of Fig. 2 compare the axial distributions of spectrally-integrated radiative intensity computed with the NB model with and without considering the methanol radiation (NB: No Fuel vs. NB: $CH_3OH$). For both pool fires, the peak of radiative intensity is enhanced when methanol radiation is considered owing to an increase in radiative emission in the hot dome region located beyond the peak. Below the peak, i.e. in the cold fuel rich region, fuel absorption becomes dominant which explains why the radiative intensities decrease in a non-negligible manner while decreasing $z$ in the "NB: $CH_3OH$" calculations. The rate of decrease is higher for the 1 m pool. These results suggest that the methanol radiation affects radiative heat transfer through competitive mechanisms: an enhancement in radiative emission in the hot part of the fuel dome and an enhancement of radiative absorption at vicinity of the fuel surface. For both the 30 cm and 1 m pool fire, the enhancement in emission overall prevails, leading to a higher radiative intensity at the fuel surface when methanol radiation is considered. However, the enhancement in radiative absorption close to the fuel surface is much more pronounced in the 1 m diameter pool fire owing to a longer cold zone length.

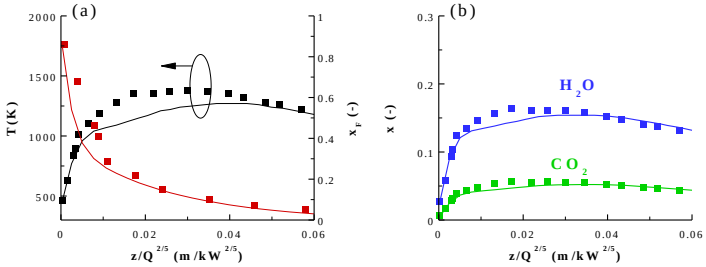


Fig. 1 Axial profiles of (a) temperature and fuel mole fraction and (b) $CO_2$ and $H_2O$ mole fractions in the fuel rich core of the flame as a function of $z/\dot{Q}^{2/5}$ for the 30 cm pool (continuous lines) and the 1 m pool (symbols).

The right frames of Fig. 2 report the incident NB spectral radiative intensity at the pool surface as a function of the wavelength for the two pool fires. Methanol participates radiatively through four spectral bands: (i) The OH stretching band between about 2.6 and 2.8 $\mu$m that interacts with the $CO_2/H_2O$ spectrum, (ii) the CH stretching band between about 3.1 and 3.7 $\mu$m that interacts weakly with the $CO_2/H_2O$ spectrum, (iii) the CH bending band between about 6.2 and 9.1 $\mu$m that interacts with the $CO_2/H_2O$ spectrum, and (iv) CO stretching band that weakly interacts with the $CO_2/H_2O$ spectrum. For the 30 cm pool, the enhancement in radiative emission due to methanol is strongly dominating. A consequence is that the radiative intensity at the pool surface is higher at all the wavelengths when methanol radiation is considered (see Fig. $2a_2$). For the 1 m pool fire, the effects of the strong methanol absorption manifests clearly on the bands where methanol and $CO_2/H_2O$ interact, with the spectral intensity becoming lower in the case with methanol radiation (see Fig. $2b_2$).

*4.4.3 Full-spectrum k distribution models*

Although the illustration, Predictions obtained with the RCFSK are also reported in the left frames of Fig. 2 for $T_p$ =1500 K and a Gauss-Legendre quadrature scheme with $N_g = 32$ points. The RCFSK scheme preserves emission and is weakly dependent on the Planck temperature $T_p$ in the range 1000-2000 K [31]. As a consequence, $T_p$ was set to 1500 K. When fuel radiation is disregarded (simulations labelled No Fuel), the RCFSK scheme predicts axial profiles of radiative intensity in a remarkable agreement with the NB solutions. When fuel radiation is

considered (simulations labelled $CH_3OH$), the RCFSK provides accurate solutions in the emission-dominated region but overestimates the absorption in the cold fuel rich part of the fuel dome. These discrepancies are enhanced while increasing the pool diameter due to an enhancement in fuel absorption. They can be attributed the underlying assumption of "rank-correlated spectra" in the RCFSK that is no longer valid in configurations where radiation emitted from $CO_2/H_2O$ mixtures is absorbed by methanol. Figure 2 shows the predictions the MSRCFSK also obtained with $T_p$ =1500 K and $N_g$ = 32. The MSRCFSK has a similar accuracy as the NBCK for spectrally-integrated intensity and appears to be a good candidate to be implemented in LES simulations of pool fires. Nevertheless, the model has to be optimized in order to make these simulations affordable.

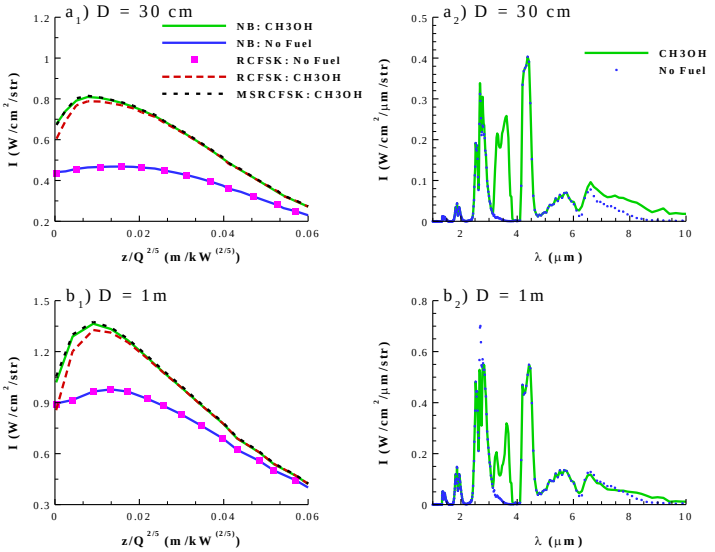


Fig. 2 NB and FS simulations of radiative heat transfer along the axis of (a) 30 cm and (b) 1 m methanol pool fires. The left (index 1) and right (index 2) panels represent the integrated intensity along the line of sight and the NB spectral intensity at the pool surface and, respectively.

*4.4.4 Optimization and implementation of the MSRCFSK for LES*

The left panels of Fig. 3 investigate the effects of the number of quadrature points on the predictions of the MSRCFSK. It can be observed that the predicted radiative intensity profiles are almost indistinguishable as the number of quadrature points is reduced from 32 to 8. The results obtained with $N_g$ =5 also exhibit an excellent accuracy, with a maximum relative error of 2.48% as compared to the case of $N_g$ =32, observed for the 30 cm pool fire. The solutions with $N_g$ =4 remain acceptable, being within 5% of those obtained with $N_g$ =32. For LES $N_g$ is selected equal to 5 to provide the best compromise between accuracy and computational efficiency. This results in 5 RTEs to solve for each scale, i.e. a total of 10 RTEs. The right panels of Fig. 3 show that the MSRSCFK solutions are almost insensitive to the Planck temperature in the range 1000-2000K and only small discrepancies are observed for $T_p = 500$ K. These results confirm the conclusions drawn for the RCFSK method [31], i.e. the Planck temperature can be fixed to a constant temperature in the range 1000-2000K. This conclusion has two important implications. The first one is that it avoids the uncertainty related to the definition of a relevant reference temperature, especially in the case of turbulent flames. The second one is that $k^\star$, $a$,

and $\lambda$ depend only on local scalars, namely $x_{CO2}$, $x_{H2O}$, $x_F$ and $T$. Consequently, these quantities can be efficiently stored in a look-up table as they can be expressed only in terms of $Z$, $\chi$ and $X_R$. In the present study, $T_p$ is set equal to 1500 K consistently with our previous studies [11,12].

The MSRCSK was further tested by considering radiative heat transfer through a line of sight corresponding to a snapshot of axial distributions of concentration and temperature for the 1 m methanol pool fire. The conclusion drawn in the present section, i.e. that a good accuracy can be achieved by setting $N_g$ =5 and $T_p$ =1500 K, was found to remain valid. This is illustrated in the section S2 of the supplementary materials.

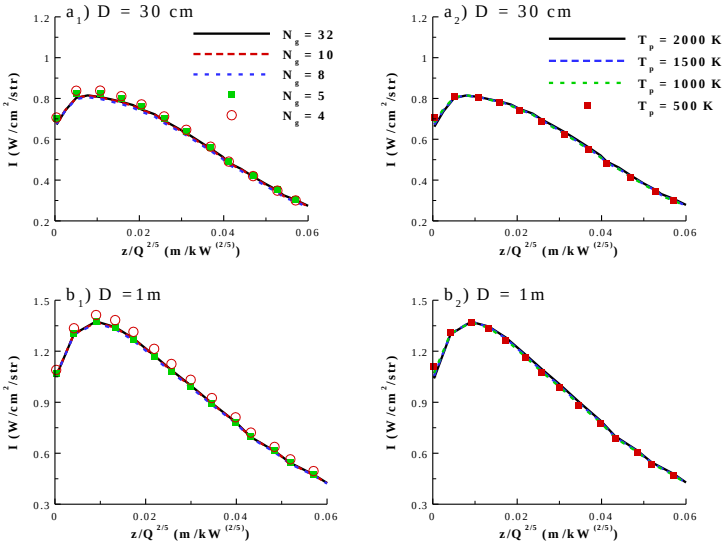


Fig. 3 Optimization of the MSRCSFK. The left (index 1) and right (index 2) panels quantify the effects of the number of quadrature points and Planck temperature on the radiative intensity along the flames' axis, respectively.

In the LES framework, the filtered FS RTE for both the mixing and methanol scales are derived from Eqs. 8a and 8b, leading to:

$$\frac{d\overline{I_{mix,g_0}}}{ds} = \overline{k^{\star}_{mix}(g_0)a_{mix}(g_0)I_b(T)} - \overline{\lambda_{mix}(g_0)I_{mix,g_0}} \quad (10a)$$

$$\frac{d\overline{I_{F,g_0}}}{ds} = \overline{k^{\star}_{F}(g_0)a_{F}(g_0)I_b(T)} - \overline{\lambda_{F}(g_0)I_{F,g_0}} \quad (10b)$$

The filtered absorption terms, $\overline{\lambda_{m,go}\mathrm{I}_{m,go}}$, is closed by neglecting the SGS absorption Turbulence Radiation Interaction (TRI), leading to $\overline{\lambda_{m,go}I_{m,go}} \approx \overline{\lambda_{m,go}}\,\overline{I_{m,go}}$. This approximation was found to be valid in LES of non-luminous and luminous lab- and large-scale diffusion flames in which about 80% of the turbulent fluctuations are resolved [32,33] as those performed in the present study. On the other hand, previous studies demonstrated the importance of SGS emission TRI for similar resolutions [13,34]. The emission terms and the overlap parameters depend only on temperature and mole fractions of $CO_2$, $H_2O$ and $CH_3OH$. Therefore, the filtering operation for these terms can be performed accurately by using the FDF approach (see Eq. 1):

$$\overline{k^{\star}_{m,g0}a_{m,g0}I_b} = \bar{\rho}\int_0^1 \frac{\left(k^{\star}_{m,g0}a_{m,g0}I_b\right)^{fl}(Z,\widetilde{\chi},\widetilde{X_R})}{\rho^{fl}(Z,\widetilde{\chi},\widetilde{X_R})}\beta\left(Z;\tilde{Z},V_z\right)dZ \quad (11a)$$

$$\overline{\lambda_{m,g0}} = \bar{\rho}\int_0^1 \frac{\left(\lambda_{m,g0}\right)^{fl}(Z,\widetilde{\chi},\widetilde{X_R})}{\rho^{fl}(Z,\widetilde{\chi},\widetilde{X_R})}\beta\left(Z;\tilde{Z},V_z\right)dZ \quad (11b)$$

$\overline{k^{\star}_{m,g0}a_{m,g0}I_b}$ and $\overline{\lambda_{m,g0}}$ are stored a priori in a library for each scale $m$ and each quadrature point $g_0$ as function of $\tilde{Z}$, $V_z$, $\tilde{\chi}$ and $\widetilde{X_R}$ and are interpolated during the LES based on the local values of these parameters. The filtered RTE is solved at each time step by using the Finite Volume Method with a 16×24 angular mesh and the computed filtered intensity is used to determine the radiative outputs such as the radiative source term in the energy equation, the radiative fluxes, and the radiant fraction. It should be pointed out that the reflection at the fuel surface was neglected as it represents 5-8% of the incident flux at the pool surface [1].

## 5. LES calculations

### 5.1 Radiant fraction and heat feedback to the surface

Consistently with the experiments performed by Kim et al. [19] and Sung et al. [20] on the 30 cm and 1 m methanol pool fires, the radiant fraction, $\chi_{rad}$, is decomposed into two contributions: the part of the idealized HRR radiated to the surroundings, $\chi_R$, and the part of the idealized HRR radiated toward the burner, $\chi_{sR}$:

$$\chi_{rad} = \chi_R + \chi_{sR} = \frac{\dot{Q}_R}{\dot{Q}} + \frac{\dot{Q}_{sR}}{\dot{Q}} \quad (12)$$

with

$$\dot{Q}_R = 2\pi\int_{R=D/2}^{R_0} \dot{q}''_{R,z}(r,0)rdr + 2\pi R_0\int_0^{z_0} \dot{q}''_{R,r}(R_0,z)dz \quad (13)$$

$$\dot{Q}_{sR} = 2\pi\int_0^{R} \dot{q}''_{R,z}(r,0)rdr \quad (14)$$

where $R_0$ and $z_0$ delimit a cylindrical control surface surrounding the pool fire and $\dot{q}''_{R,z}(r,0)$ and $\dot{q}''_{R,r}(R_0,z)$ represent the radial distribution of the radiative heat flux in the downward direction and the vertical distribution of radiative flux at a distance $R_0$ from the pool axis, respectively. The values of $R_0$ and $z_0$ were chosen in the simulations to match the experimental ones, i.e. $R_0 = 0.6$ m and $z_0 = 1.5$ m for the 30 cm pool fire [19] and $R_0 = 2.07$ m and $z_0 = 1.8$ m for the 1 m pool fire [20]. In addition, the heat feedback fraction, $\chi_s$, that represents the fraction of the idealized HRR retroceded to the fuel surface, can be decomposed into a radiative contribution and a convective contribution, $\chi_{conv,s}$:

$$\chi_s = \chi_{sR} + \chi_{s,conv} \quad (15)$$

with

$$\chi_{s,conv} = \frac{2\pi\int_0^R \dot{q}''_{s,conv}rdr}{\dot{Q}} \quad (16)$$

In the present study the convective contribution is obtained from stagnant layer theory [35]:

$$\dot{q}''_{conv,s} = \frac{h}{c_p}\left[(1-\chi_r)s\Delta h_C - c_p(T_b - T_\infty)\right]\frac{\dot{m}'' c_P/h}{\exp(\dot{m}'' c_P/h)-1}\left[1-\left(\frac{r}{R}\right)^5\right] \quad (17)$$

where $h$ is the convective coefficient taken equal to 8.5 W/m$^2$ in accordance with Kim et al. [19] and $c_p$, $s$, $\Delta h_c$ and $\dot{m}''$ represent the heat capacity of air, the stoichiometric fuel to air mass ratio, the heat of combustion and the burning rate per unit area. The use of the stagnant layer theory is based on the conclusions drawn by Maragkos et al. [35] that it is only slightly grid sensitive and provides satisfactory predictions for the different fuels tested.

### 5.2 The 30 cm diameter pool fire

Let us analyze first the results obtained for 30 cm pool fire. Table 2 shows that that $\chi_R$ and $\chi_{rad}$ predicted with and without considering fuel radiation are within the experimental uncertainties. When methanol radiation is considered, these two quantities are increased by about 13.5%. This increase in radiative loss due to methanol radiation is further analyzed in Fig. 4 that shows the divergence of the radiative flux, $\boldsymbol{\nabla \cdot \dot{q}''_R}$ , along the flame axis. As expected, it can be observed that methanol radiation contributes to enhance $\boldsymbol{\nabla \cdot \dot{q}''_R}$, expect close to the pool surface where $\boldsymbol{\nabla \cdot \dot{q}''_R}$ is slightly lower but still positive when methanol is considered. These trends are consistent with those described in Section 4.4.2 in the case of decoupled radiative calculations along the flame axis. Table 2 also shows that the radiative component of the fractional heat feedback to the fuel surface, $\chi_{sR}$, is significantly lower than that estimated experimentally when fuel radiation is disregarded. A better agreement is observed when fuel radiation is considered, although $\chi_{sR}$ remains underestimated. A consequence is that considering fuel radiation improves the predictions of the fractional heat feedback to the fuel surface, $\chi_s$. This is further illustrated in Fig. 5 that shows the total heat flux (radiation + convection) retroceded by the flame to the fuel surface.

Table 2. Radiant fraction and heat feedback metrics for the 30 cm methanol pool fire.

| | $\boldsymbol{\chi_{rad}}$ | $\boldsymbol{\chi_R}$ | $\boldsymbol{\chi_{sR}}$ | $\boldsymbol{\chi_s}$ |
|---|---|---|---|---|
| No Fuel | 0.235 | 0.197 | 0.0387 | 0.0653 |
| $CH_3OH$ | 0.267 | 0.224 | 0.0425 | 0.0686 |
| Exp. [19] | 0.24 $\pm$ 25% | 0.19 $\pm$ 26% | 0.055 $\pm$ 21% | 0.082 $\pm$ 24% |

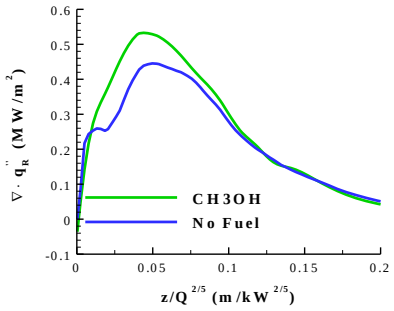


Fig. 4 Axial profiles of the divergence of the radiative flux for the 30 cm diameter pool fire.

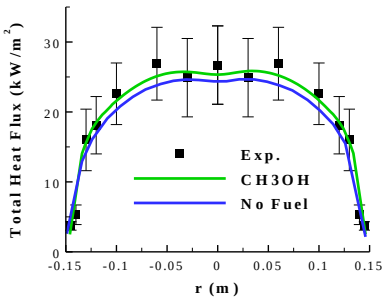


Fig. 5 Total heat feedback to the fuel surface for the 30 cm diameter pool fire. The experimental data are taken from Ref. [19].

Figure 6 shows the radial profiles of mean temperature at different heights above the pool surface predicted with and without considering methanol radiation. In both cases, the experimental profiles are well reproduced by the model. A noticeable dip is observed in the simulation and not in the experiments in the lower part of the flame. It can be reasonably attributed to the fact that the profile of the fuel injection velocity over the pan is imposed uniform in the simulation and may not match perfectly the experimental one. On the other hand, it can be observed that considering methanol radiation affects noticeably the temperature predictions. The induced increase in radiative loss leads to lower temperature, especially along the wings of the profiles for the heights higher than 10 cm which results in an overall better agreement with the experimental data.

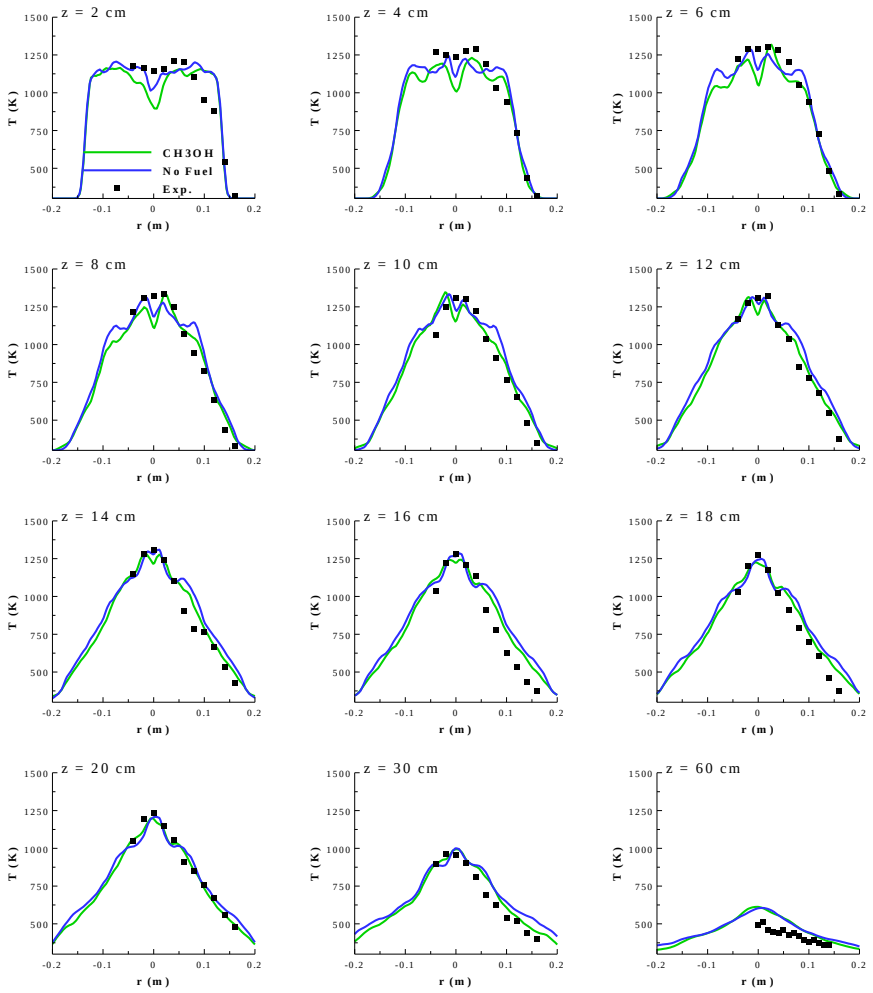


Fig. 6 Radial profiles of mean temperature at different heights for the 30 cm pool fire. The experimental data are taken from Ref. [17], except the radial profile at z=0.6 m that is taken from Ref. [18].

### 5.3 The 1 m diameter pool fire

Table 3 shows that the radiant fractions predicted with and without considering methanol radiation in the 1 m diameter methanol pool fire agree well with the experimental data. The contribution of methanol increases the total radiative loss by about 4.2%, which is significantly lower than for the 30 cm diameter pool. This behavior is consistent with the observations made in Section 4.4.2 in decoupled radiative calculations along the flame axis and can be further emphasized by comparing Figs. 4 and 7. These figures confirm that methanol radiation affects the divergence of the radiative flux through competitive effects: an enhancement of radiative emission in the hot part of the fuel dome and an enhancement of radiative absorption in the cold fuel rich region of the fuel dome located close to the fuel surface.

For the 30 cm pool fire, the enhancement of emission is highly dominating (see Fig. 4). For the 1 m diameter pool, a strong absorption by methanol is observed at the vicinity of the fuel surface (see Fig. 7), with $\boldsymbol{\nabla \cdot \dot{q}''_R}$ becoming highly negative in this region when methanol radiation is considered. A consequence is that the radiative component of the fraction of heat feedback,

$\chi_{rs}$ , is not significantly affected by methanol radiation (see Table 3). Nevertheless, Fig. 8 shows that the incident radiative flux at the fuel surface is in better agreement with the experimental data when methanol radiation is considered. Figure 9 shows the radial profiles of temperature at different heights. The model reproduces well the experiments whether fuel radiation is considered or not. Methanol radiation enhances the overall radiative loss which tends to reduce slightly the temperature, especially along the flame wings.

Table 3. Radiant fraction and radiative component of the fractional heat feedback for the 1 m methanol pool fire.

| | $\chi_{rad}$ | $\chi_{rs}$ |
|---|---|---|
| No Fuel | 0.237 | 0.0651 |
| $CH_3OH$ | 0.247 | 0.0659 |
| Exp. [19] | 0.22 $\pm$ 16% | 0.065 ± 31% |

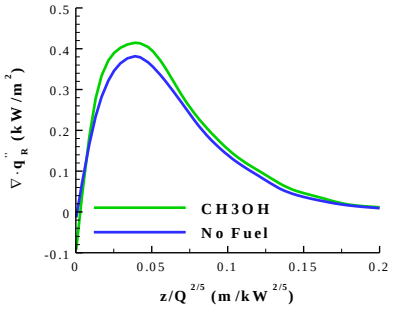


Fig. 7 Axial profiles of the divergence of the radiative flux for the 1 m diameter pool fire.

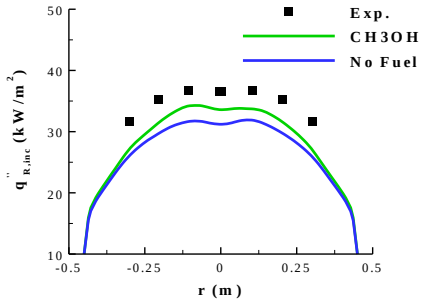


Fig. 8 Radiative heat feedback to the fuel surface for the 1 m diameter pool fire. The experimental data are taken from Ref. [21].

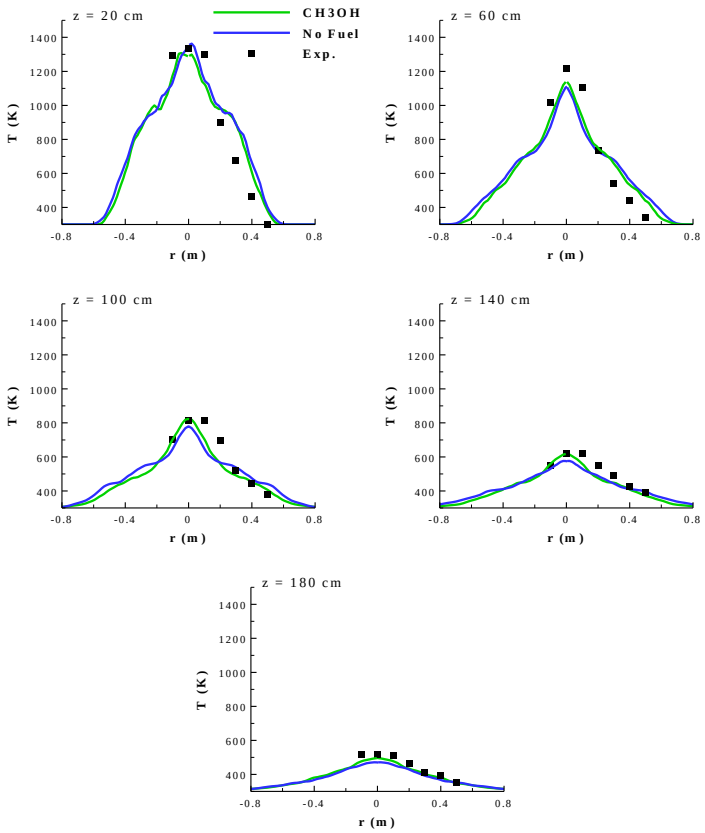


Fig. 9 Radial profiles of mean temperature at different heights for the 1 m pool fire. The experimental data are taken from Ref. [20].

### 5.4 Effects of the puffing motion on the radiative heat feedback

Figure 10 shows the distribution of the mean incident radiative flux at the fuel surface for the two pool fires. The bars represent the level of the fluctuations of the incident radiative flux at the different locations.

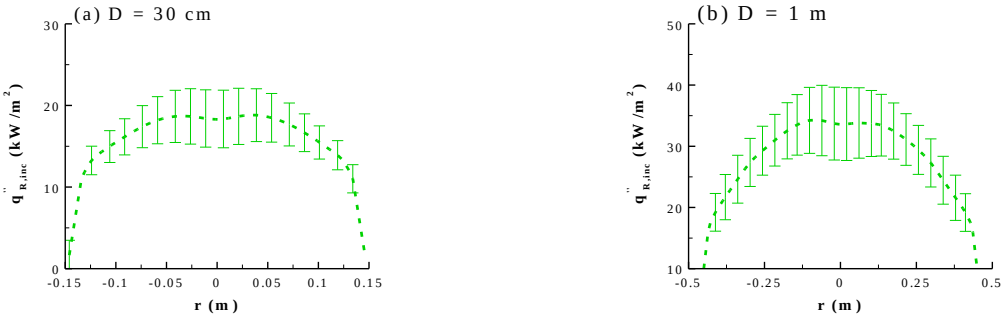


Fig. 10 Radiative heat feedback to the fuel surface for the (a) 30 cm pool fire and (b) 1 m diameter pool fire. The bars represent the rms of the radiative feedback fluctuations. The simulations account for the fuel contribution to radiative heat transfer.

These fluctuations represent approximately 20 % of the mean value at the pool center for both pool fires and this percentage decreases slightly toward the edge to reach about 14-15%. A careful analysis of the time series of the incident radiative flux shows that it fluctuates at a frequency similar to the puffing frequency of 2.8 Hz and 1.25 Hz for the 30 cm [11] and 1 m [12] pool fires, respectively. These fluctuations should affect in turn the mass burning rate through the energy balance at the fuel surface.

## 6. Conclusions

This article proposes an optimized MSRCFSK to model accurately the radiative heat transfer in the fuel rich core located above vaporizing liquid or solid fuels and the resulting radiative heat feedback to the fuel surface. This model has been implemented in a well-validated numerical model to perform LES of 30 cm and 1 m diameter methanol pool fires. The following conclusions can be drawn:

- The MSRCFSK provides a similar accuracy as the NBCK model for spectrally-integrated radiative properties.
- The MSRCFSK is weakly sensitive to the number of quadrature points and accurate predictions can be achieved with 5 quadrature points for each scale, resulting in a total of 10 RTEs to be solved.
- The MSRCFSK is weakly sensitive to the Planck temperature that can be fixed to a constant value in the range 1000-2000 K. A consequence is that the MSRCFSK radiative parameters depend then only on local scalars and can be efficiently stored in a library as function of the flamelet parameters.
- The contribution of methanol to radiative heat transfer results from competitive mechanisms: an increase in radiative emission in the hot part of the fuel dome and an increase in radiative absorption in the cold part close to the pool surface. For both pool fires, the enhancement in emission dominates leading to higher overall radiative loss and heat feedback to the fuel surface and to slightly lower mean temperature. However, the contribution of absorption in the cold region of the pool increases with the pool size, and the effects of methanol radiation are much more pronounced for the 30 cm pool than for the 1 m one. These results suggest that the fuel blockage will increase with the pool size. In addition, the experiments conducted by Suo-Antilla et al. [3] suggest that the fuel radiation blockage may be more significant for sooting fuels.
- Considering the contribution of methanol to radiative heat transfer improves the predictions of the heat feedback to the fuel surface.

It should be pointed out that three kind of measurements would be useful to improve the modelling of the fuel radiative blockage: i) reproduce the narrow band measurements for the fuel made by Wakatsuki [7] for higher optical thicknesses in order to refine the statistical narrow band parameters, ii) to measure systematically the radiative heat feedback in pool fire experiments, and iii) to measure flame spectral radiative intensity along a line-of-sight as reported by Suo-Antilla et al. [3].

## References

[1] A. Hamins, S.J. Fischer, T. Kashiwagi, M.E. Klassen, J.P. Gore, Heat feedback to the fuel surface in pool fires, Combust. Sci. Technol. 97 (1994) 37–62. https://doi.org/10.1080/00102209408935367.

[2] K. Wakatsuki, G.S. Jackson, A. Hamins, M.R. Nyden, Effects of fuel absorption on radiative heat transfer in methanol pool fires, Proc. Combust. Inst. 31 (2007) 2573-2580. https://doi.org/10.1016/j.proci.2006.08.049.
[3] J.M. Suo-Anttila, T.K. Blanchat, A.J. Ricks, A.L. Brown, Characterization of thermal radiation spectra in 2 m pool fires, Proc. Combust. Inst. 32 (2009) 2567–2574. https://doi.org/10.1016/j.proci.2008.06.044.
[4] L. Rothman, I. Gordon, R. Barber, H. Dothe, R. Gamache, A. Goldman, et al., HITEMP, the high-temperature molecular spectroscopic database. J. Quant. Spectrosc. Radiat. Transf. 111 (2010) 2139-50. https://doi.org/10.1016/j.jqsrt.2010.05.001.
[5] I.E. Gordon, L.S. Rothman, R.J. Hargreaves, R. Hashemi, E.V. Karlovets, et al., The HITRAN2020 molecular spectroscopic database, J. Quant. Spectrosc. Radiat. Transf. 277 (2022) 107949. https://doi.org/10.1016/j.jqsrt.2021.107949.
[6] J.L. Consalvi, F. Liu, A database of narrow-band parameters for fuels commonly encountered in fire applications, Fire Safety J. 78 (2015) 202-218. https://doi.org/10.1016/j.firesaf.2015. 10.002.
[7] K. Wakatsuki, High temperature radiation absorption of fuel molecules and an evaluation of its influence on pool fire modeling, Ph.D. thesis, University of Maryland, USA, 2005.
[8] V.R. Lecoustre, K. Wakatsuki, G.S. Jackson, Fitting narrow-band models to temperature-dependent, spectral absorption coefficients of fuel vapors, J. Quant. Spectrosc. Radiat. Transf. 147 (2014) 24-37. https://doi.org/10.1016/j.jqsrt.2014.05.007.
[9] H. Sadeghi, S. Hostikka, G. Crivelli Fraga, H. Bordbar, Weighted-sum-of-gray-gases models for non-gray thermal radiation of hydrocarbon fuel vapors, $CH_4$, CO and soot, Fire Safety J. 125 (2021) 103420. https://doi.org/10.1016/j.firesaf.2021.103420.
[10] M.F Modest, S. Mazumder, Radiative heat transfer, Academic Press, 2021.
[11] L. Ma, F. Nmira, J.L. Consalvi, Large Eddy Simulation of medium-scale methanol pool fires - effects of pool boundary conditions, Combust. Flame 222 (2020) 336-354. https://doi.org/10.1016/j.combustflame.2020.09.007.
[12] F. Nmira, L. Ma, J.L. Consalvi, Influence of gas radiative property models on Large Eddy Simulation of 1 m methanol pool fires, Combust. Flame 221 (2020) 352-363. https://doi.org/10.1016/j.combustflame.2020.08.005.
[13] F. Nmira, J.L. Consalvi, Local contributions of resolved and subgrid turbulence-radiation interaction in LES/presumed FDF modelling of large-scale methanol pool fires, Int. J. Heat Mass Transf. 190 (2022) 122746. https://doi.org/10.1016/j.ijheatmasstransfer.2022.122746
[14] H. Zhang, M.F. Modest, A multi-scale full-spectrum Correlated-k distribution for radiative heat transfer in inhomogeneous gas mixtures, J. Quant. Spectrosc. Radiat. Transfer 73 (2002) 349-360. https://doi.org/10.1016/S0022-4073(01)00220-5.
[15] L. Wang, M.F. Modest, Narrow-band based multiscale full-spectrum k-distribution method for radiative transfer in inhomogeneous gas mixtures, J. Heat. Transfer 127 (2005) 740-748. https://doi.org/10.1115/1.1925281.
[16] J.L. Consalvi, F. Liu, Radiative heat transfer in the core of axisymmetric pool fires – I: Evaluation of approximate radiative property models, Int. J. Thermal Sci. 84 (2014) 104-117. https://doi.org/10.1016/j.ijthermalsci.2014.04.018.
[17] E.J. Weckman, A.B. Strong, Experimental investigation of the turbulence structure of medium-scale methanol pool fires, Combust. Flame 105 (1996) 245-266. https://doi.org/10.1016/0010-2180(95)00103-4.

[18] A. Hamins, A. Lock, The structure of a moderate-scale methanol pool fire, NIST Technical Note (2016) 1928.
[19] S.C. Kim, K.Y. Lee, A. Hamins, Energy balance in medium-scale methanol, ethanol, and acetone pool fires, Fire Safety J. 107 (2019) 44-53. https://doi.org/10.1016/j.firesaf.2019.01.004.
[20] K. Sung, J. Chen, M. Bundy, A. Hamins, The characteristics of a 1 m methanol pool fire, Fire Safety J. 120 (2021) 103121. https://doi.org/10.1016/j.firesaf.2020.103121.
[21] M. Klassen, J.P. Gore, Structure and radiation properties of pool fires, NIST-GCR-94-651, NIST, 1992.
[22] http://www.iafss.org/macfp/.
[23] http://www.code-saturne.org
[24] J. Li, Z. Zhao, A. Kazakov, M. Chaos, F.L. Dryer, J.J. Scire Jr., A comprehensive kinetic mechanism for CO, $CH_2O$, and $CH_3OH$ combustion, Int. J. Chem. Kinet. 39 (2007) 109-136. https://doi.org/10.1002/kin.20218
[25] C. Jiménez, F. Ducros, B. Cuenot, B. Bédat, Subgrid scale variance and dissipation of a scalar field in large eddy simulations, Phys. Fluids 13 (2001) 1748-1754. https://doi.org/10.1063/1.1366668
[26] J. Pearson. The development of updated and improved SLW model parameters and its application to comprehensive combustion prediction, PhD dissertation, Brigham Young University, Provo, UT, 2013.
[27] F. André, R. Vaillon, The k-moment method for the narrow band modeling of radiative properties of nonuniform gaseous media, J. Quant. Spectrosc. Rad. Transf. 109 (2008) 258-268. https://doi.org/10.1016/j.jqsrt.2007.08.014
[28] A.A. Lacis, V.A. Oinas, Description of the correlated-k distribution method for modeling nongray gaseous absorption, thermal emission, and multiple scattering in vertically inhomogeneous atmospheres, J. Geophys. Res. 96 (1991) 9027-9063. https://doi.org/10.1029/90JD01945.
[29] M.F. Modest, R.J. Riazzi, Assembly of full-spectrum k-distributions from a narrow-band database; effects of mixing gases, gases and nongray absorbing particles, and mixtures with nongray scatterers in nongray enclosures, J. Quant. Spectrosc. Radiat. Transf. 90 (2005) 169–189. https://doi.org/10.1016/j.jqsrt.2004.03.007.
[30] V.P. Solovjov, B. W. Webb, F. Andre, The Rank Correlated FSK model for prediction of gas radiation in non-uniform media, and its relationship to the Rank Correlated SLW Model, J. Quant. Spectrosc. Radiat. Transf. 214 (2018) 2018. https://doi.org/10.1016/j.jqsrt.2018.04.026
[31] J.L. Consalvi, F. Andre, F.R. Coelho, F.H.R. Franca, F. Nmira, M. Galtier, V. Solovjov, B.W. Webb, Assessment of engineering gas radiative property models in high pressure turbulent jet diffusion flames, J. Quant. Spectrosc. Radiat. Transfer 253 (2020) 107169. https://doi.org/10.1016/j.jqsrt.2020.107169
[32] A. Gupta, D.C. Haworth, M.F. Modest, Turbulence-radiation interactions in large eddy simulations of luminous and nonluminous nonpremixed flames, Proc. Combust. Inst. 34 (2013) 1281–1288. https://doi.org/10.1016/j.proci.2012.05.052
[33] J.L. Consalvi, F. Nmira, W. Kong, On the modeling of the filtered radiative trans- fer equation in large eddy simulations of lab-scale sooting turbulent diffusion flames, J. Quant. Spectrosc. Radiat. Transf. 221 (2018) 51–60. https://doi.org/10.1016/j.jqsrt.2018.09.020
[34] F. Nmira, L. Ma, J.L. Consalvi, Assessment of subfilter-scale turbulence-radiation interaction in non-luminous pool fires, Proc. Combust. Inst. 38 (2021) 4927-4934. https://doi.org/10.1016/j.proci.2020.06.271

[35] G. Maragkos, B. Merci, Grid insensitive modelling of convective heat transfer fluxes in CFD simulations of medium-scale pool fires, Fire Safety J. 120 (2021) 103104. https://doi.org/10.1016/j.firesaf.2020.103104

**Figure captions**

Fig. 1 Axial profiles of (a) temperature and fuel mole fraction and (b) $CO_2$ and $H_2O$ mole fractions in the fuel rich core of the flame as a function of $z/\dot{Q}^{2/5}$ for the 30 cm pool (continuous lines) and the 1 m pool (symbols).

Fig. 2 NB and FS simulations of radiative heat transfer along the axis of (a) 30 cm and (b) 1 m methanol pool fires. The left (index 1) and right (index 2) panels represent the integrated intensity along the line of sight and the NB spectral intensity at the pool surface and, respectively.

Fig. 3 Optimization of the MSRCSFK. The left (index 1) and right (index 2) panels quantify the effects of the number of quadrature points and Planck temperature on the radiative intensity along the flames' axis, respectively.

Fig. 4 Axial profiles of the divergence of the radiative flux for the 30 cm diameter pool fire.

Fig. 5 Total heat feedback to the fuel surface for the 30 cm diameter pool fire. The experimental data are taken from Ref. [19].

Fig. 6 Radial profiles of mean temperature at different heights for the 30 cm pool fire. The experimental data are taken from Ref. [17], except the radial profile at z=0.6 m that is taken from Ref. [18].

Fig. 7 Axial profiles of the divergence of the radiative flux for the 1 m diameter pool fire.

Fig. 8 Radiative heat feedback to the fuel surface for the 1 m diameter pool fire. The experimental data are taken from Ref. [21].

Fig. 9 Radial profiles of mean temperature at different heights for the 30 cm pool fire. The experimental data are taken from Ref. [20].

Fig. 10 Radiative heat feedback to the fuel surface for the (a) 30 cm pool fire and (b) 1 m diameter pool fire. The bars represent the rms of the radiative feedback fluctuations. The simulations account for the fuel contribution to radiative heat transfer.